FIBRE-REINFORCED SAND: INTERACTION AT THE FIBRE AND GRAIN SCALE

A. Diambra, E. Ibraim

Queen's School of Engineering, University of Bristol, Bristol, United Kingdom

ABSTRACT

For fibre reinforced granular soils, the efficiency of the fibres is governed by the local fibre-grain interaction mechanism. This local interaction mechanism is evaluated, in this paper, by using a modified version of the shear-lag stress theory. While this theory provides a description of the stress-transfer mechanism at fibre-matrix interface level, it also generates the stress distribution along the fibre. The proposed model explicitly accounts for the effects of the geometrical fibre and granular size characteristics, fibre stiffness, global stress level, soil density and the non-linearity of soil behaviour. An analytical expression for the ratio of strains in the fibre and in the composite, which is fundamental for any prediction of fibre contribution, is further derived. A discussion on the effects of the controlling parameters is presented, while the scale-up of the problem at the composite level is then conducted by using a continuum constitutive model (like that proposed by Diambra et al., 2013) appropriately modified to account for the strain ratio between the fibre and the composite. The model is validated against a series of triaxial compression tests on two different sands mixed with polypropylene fibres of different aspect ratios.

KEYWORDS: Ground improvement, Reinforced soils, Numerical modelling, Constitutive relations, Sands

1 INTRODUCTION

There is no doubt that the treatment of granular soils with discrete short fibre type inclusions can increase soil's strength while also affecting the deformation characteristics of the material. The viability of the concept has been largely demonstrated through laboratory experiments on soil sample elements loaded under various testing conditions and for a wide range of fibre types. The experimental results have confirmed that the efficiency of the fibre treatment is highly dependent on the fibre concentration, on testing conditions (e.g. stress and strain levels, stress path and loading direction) and on a large number of variables related equally to both fibre and sand matrix physical and dimensional characteristics (e.g. fibre and particle sizes and particle size distribution, particle shape and fibre surface, fibre/grain frictional properties, stiffness) as well as their spatial configuration (e.g. matrix packing and fibre orientation, fibre distribution). Among these variables, the geometrical characteristics, fibre length, fibre diameter, and the size of granular particles form a special set of inter-related parameters. Increasing the fibre aspect ratio (fibre length over fibre diameter) increases the fibre surface area which results on an enhancement of the fibre-matrix interaction efficiency (Gray and Al Refeai, 1986; Ranjan et al., 1996; Al Refeai, 1991; Consoli et al., 2007). While maintaining constant the fibre aspect ratio, the fibre reinforcement effect increases with the reduction of the particle size (Gray and Al-Refeai, 1986; Maher and Gray, 1990; Ranjan et al., 1996; Michałowski and Čermák, 2003). Michałowski and Čermák (2003) suggest that fibre length should be at least one order of magnitude higher than the grain size if the fibre-soil interaction mechanism is to be triggered. On the other hand, there seems to be an upper limit to the fibre length or fibre aspect ratio beyond which the fibre efficiency remains unchanged (Gray and Ohashi 1983, Al Refeai, 1991). The only attempt to capture in an analytical form the combined effects of fibre and grain dimensions was conducted by Lirer et al. (2012) who, relying on some basic micromechanical considerations and analogy with the work of Zornberg (2002), proposed a relation for the limiting shear strength of the fibre-reinforced soil that incorporates the fibre aspect ratio and fibre length/particle size geometrical variables. The validity of the limiting shear strength expression has been challenged against a range of published test results on various soils and fibre type mixtures.

The present paper investigates the local fibre-soil matrix interaction mechanism using a modified shear lag theory. While this theory provides a description of the stress-transfer mechanism at fibre-matrix interface level and consequently the stress distribution along the fibre, it can explicitly account for the effects of the geometrical fibre and granular size characteristics, including parameters such as the fibre stiffness, global stress level, soil density, and the non-linearity of the soil behaviour. An analytical expression for the ratio of strains in the fibre and in the composite is further proposed through the integration of the stress distribution function and the account of the fibre constitutive model. The scale-up of the problem at the composite level is then conducted by using a continuum constitutive model (like that proposed by Diambra et al., 2013) appropriately modified to account for the strain ratio between the fibre and the composite. The model is validated against a series of triaxial compression tests on two different sands mixed with polypropylene fibres with different aspect ratios.

2 TOWARDS AN EXAMINATION OF THE SOIL MATRIX – FIBRE INTERACTION MECHANISM

2.1 Introduction

A two-dimensional representation of an unstressed single fibre embedded in a continuum matrix is reported in Fig. 1a. For a pre-failure (i.e. the fibre/matrix friction resistance is not exceeded and/or the fibre has not broken yet) tensile loading applied parallel to the fibre length, since the fibre is generally stiffer than the matrix, shear distortion takes place as shown in Fig.1b (Hull and Clyne, 1996). Reference lines, initially straight and perpendicular to the fibre axis, are included to visualise the fibre-matrix deformation pattern. It is evident that the average strains of the two phases (reinforcement and matrix) do not coincide, and both shear stress and strain gradients radiate from the fibre-matrix interface. Based on equilibrium considerations and compatibility of stresses and strains between the phases, a modified shear lag theory (Cox, 1952) will be applied to assess the stress-transfer mechanism at the fibre-soil matrix interface level.

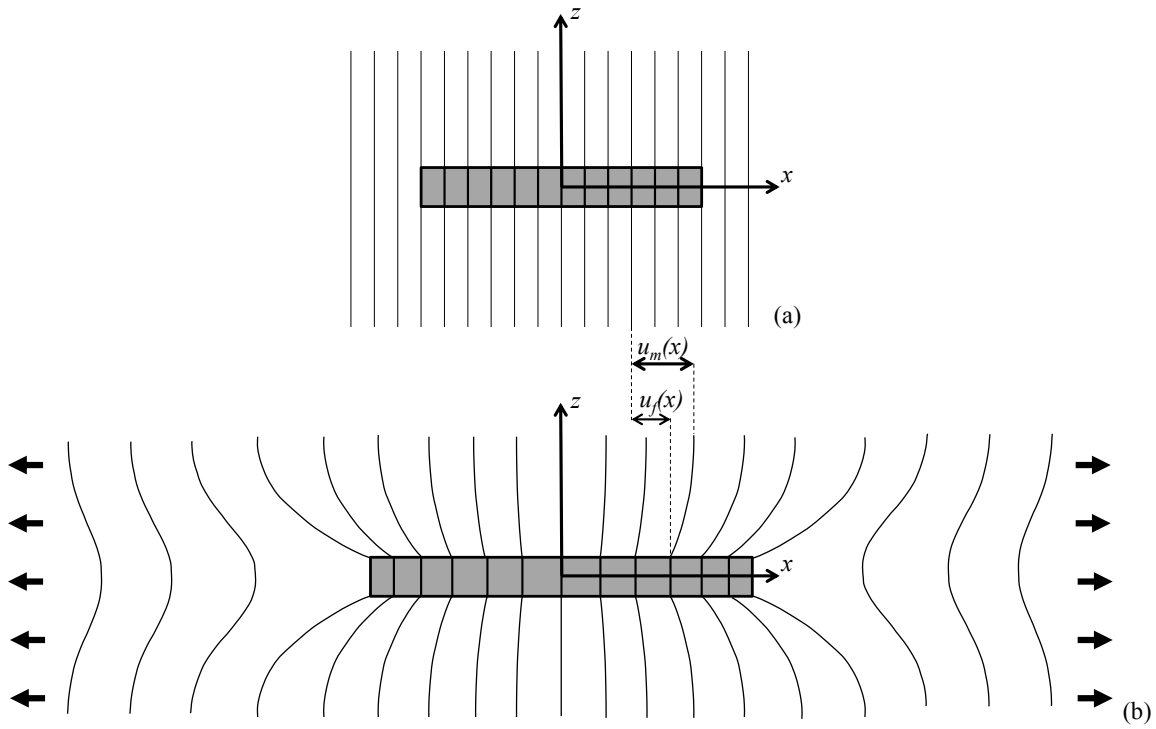

Fig.1 Two-dimensional representation of a single fibre-matrix system in (a) unstressed and (b) stressed configurations (after Hull and Clyne, 1996).

2.2 The fibre-matrix interaction mechanism model

The analysis of the fibre-matrix interaction mechanism is based on the model shown in Fig. 2a with a cylindrical fibre of radius r_f and length l_f embedded in a stress confined cylindrical volume of soil of radius R, also loaded under a tensile strain regime along the x-axis. The radius R of the cylinder can be derived to maintain an imposed given volumetric fibre concentration, μ_f, defined as volume of fibres over total composite volume, to give:

$$\frac{R}{r_f} = \sqrt{\frac{1}{\mu_f}} \qquad (1)$$

Fig. 2a also shows the stresses acting on an element of the composite, while the radial and circumferential normal stresses are not represented for the sake of clarity.

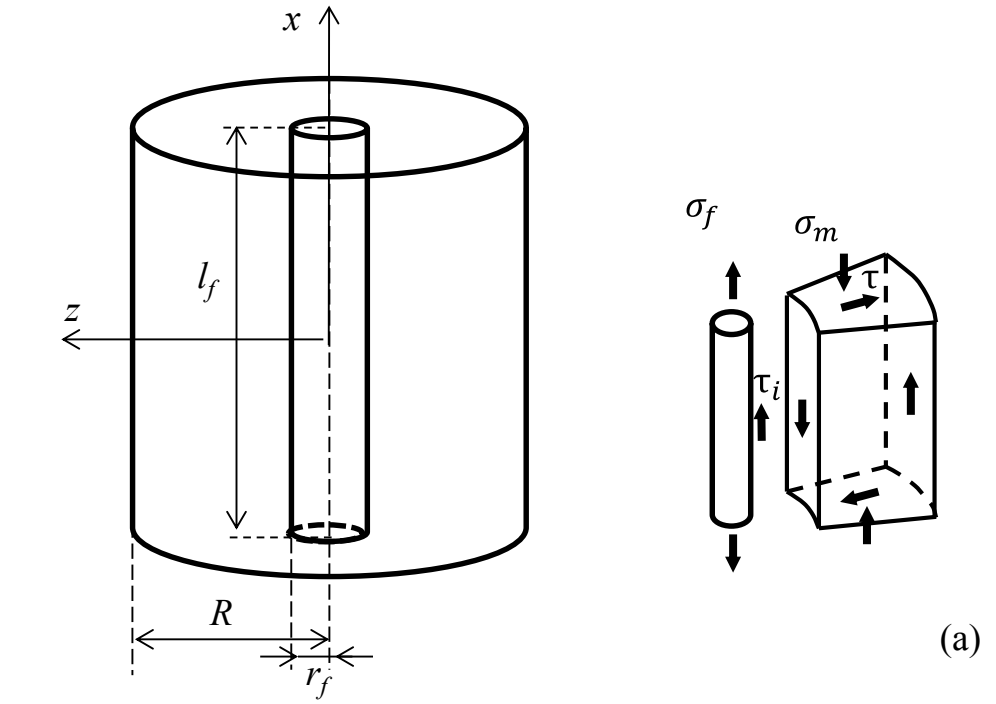

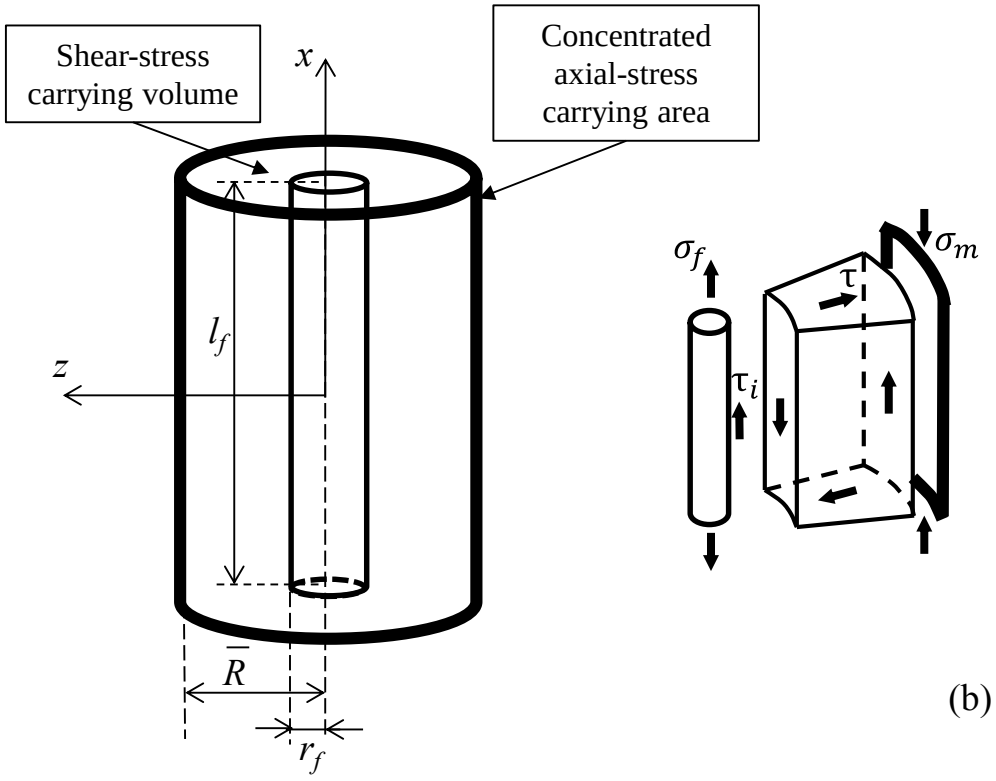

Fig. 2 Geometric representation of (a) the fibre reinforced cylinder and the general stress state of fibre and matrix elements; (b) the idealised composite model where the matrix has been separated into a concentrated axial stress carrying are and a shear-stress carrying region, and the relative stress states of the three components.

Following the approach of Aveston and Kelly (1973) and Budiansky et al. (1986), the fibre-soil model is further modified into an equivalent system where the soil matrix can be separated into two distinct de-coupled parts: a concentrated pure axial-stress carrying area, and a pure shear stress-carrying volume (Fig. 2b). To satisfy the equivalence between the systems in Figs. 2a and 2b, the axially-stressed matrix must have a cross sectional area of $\pi(R^2 - r_f^{\,2})$ and must be located at a radial coordinate z=$\bar{R}$ with r_f <$\bar{R}$<R. The pure shear stress-carrying volume extends between r_f and $\bar{R}$. Aveston and Kelly (1973) suggested taking $\bar{R}$ at the location of an average axial displacement of the matrix, while Budiansky et al. (1986) used a procedure based on the shearing energy contributions of the two equivalent systems. Most recently, Mahesh et al. (2004) stated that the distributions of the stresses and strains are quite insensitive to the precise value of $\bar{R}$ (with exception of $\bar{R}/r_f \approx 1$) and simply suggested:

$$\bar{R} = \frac{(r_f + \mathrm{R})}{2} \tag{2}$$

which actually corresponds to the Aveston and Kelly (1973) solution if a linear variation of the displacement *u* is assumed along a cross section of the matrix. Combining Eqs. (1) and (2), the size $\bar{R}$ of the shear matrix can be defined as:

$$\frac{\bar{R}}{r_f} = \frac{1}{2}\left(1 + \sqrt{\frac{1}{\mu_f}}\right) \tag{3}$$

2.3 Constitutive relationships of mixture constituents

The shear-lag theory is based on considerations about the overall equilibrium of the composite material and the compatibility of stresses and strains between the constituents. Thus, individual constitutive relationships for the fibres and the granular soil matrix will be introduced.

2.3.1 Fibre model

Fibres are assumed to be linear elastic uni-dimensional elements resistant only to tensile loading. It is assumed that their compressive and bending resistances are negligible. The tensile elastic stiffness of the fibres is defined by E_f. Although the fibre has a finite length, l_f, some recent research suggests that the interaction mechanism is actually active over a shorter fibre length: the effective length, l_f^*. Discrete

Element Modelling (DEM) simulations of idealised fibre reinforced granular material conducted by Ibraim et al. (2006) and Maeda and Ibraim (2008) have shown that there could be fibres not fully stretched over their full length even if they appear oriented along a tensile strain direction. Lirer et al. (2011), based on De Gennes (1979), considered in their derivations an effective (or actively stretched) fibre length to be equal to the square root of the true fibre length. Based on back calculation from results of direct shear tests, Gray and Ohashi (1983) showed that the tensile strength of the fibres is not fully mobilised. In addition, Michałowski and Čermák (2003) concluded that fibres need to be about an order of magnitude higher than the average grain size, D_{50}, to efficiently activate the fibre-grain interaction mechanism. Based on these observations, the following function for the effective fibre length, l_f^*, is conjectured:

$$\frac{l_f^*}{l_f} = k\,\frac{1}{1+\alpha} \tag{4}$$

with

$$\alpha = \left(b\,\frac{l_f}{D_{50}}\right)^{-m} \tag{5}$$

where m and b are shape parameters. While the choice of a function like this has the advantage of taking explicitly into account the fibre-grain scale effect, it approaches zero for low values of l_f/D_{50} (very short fibres or big particles) and it increases to an asymptotic value k for higher values of l_f/D_{50} in agreement with the experimental observations of Gray and Ohashi (1983) and Al Refeai (1991). A review of the latter results suggests that the upper asymptotic limit is reached when the ratio l_f/D_{50} exceeds a value of about 100. Thus an appropriate combination of $b=0.08$ and $m=2$ which satisfies these requirements has been adopted and the function (4) is shown in Fig.3. Note that $1/b$ is the value of l_f/D_{50} corresponding to a ratio l_f^*/l_f equal to $k/2$, while m controls the shape of the curve. The parameter k, which varies only between 0 and 1, should reflect the internal matrix fabric and fibre arrangement - difficult to quantify – and for this reason its value will result from a calibration process against experimental data.

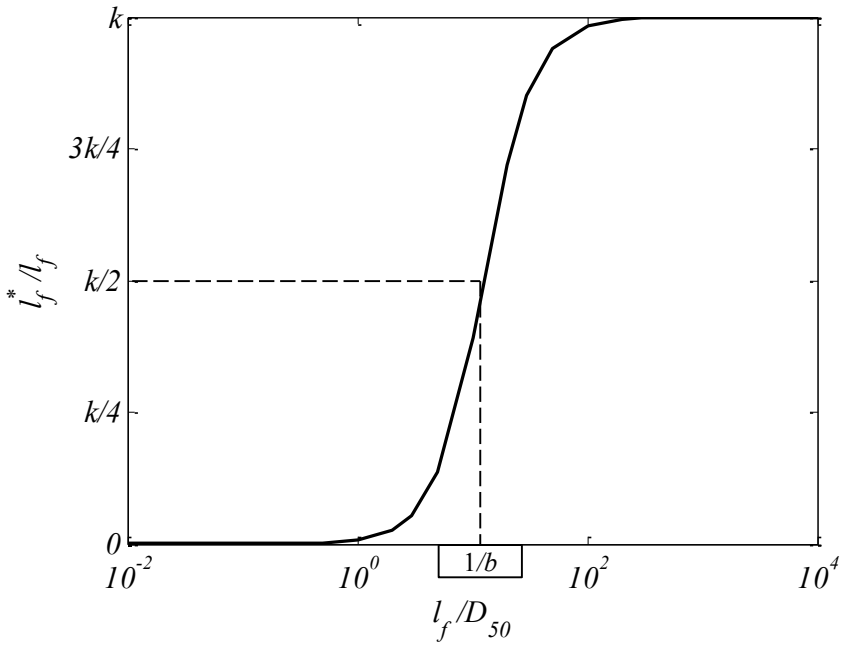

Fig.3 Graphical representation of the assumed function or the ratio between effective and true fibre length from equation (4).

2.3.2 Soil constitutive model

The developments below refer to a soil element under simple shear. The one-dimensional elasto-plastic soil model proposed by Muir Wood (2009) (a simplification of the bounding surface, kinematic hardening, Severn-Trent sand model proposed by Gajo and Muir Wood (1999)), can capture the mechanical behaviour of granular soils over a wide range of densities and stress levels. The non-linear behaviour of soils can be represented using a hyperbolic mobilisation of the shear strength with the shear strain:

$$\tau = \frac{\gamma}{\gamma+\zeta_s}\tau_u \quad (6)$$

where τ is the mobilised shear stress, τ_u is the available shear strength, γ is the shear strain and ζ_s is a parameter that controls the shear stiffness. ζ_s is linked to the initial shear stiffness G by the following relation:

$$\zeta_s = \frac{\tau_u}{G} \quad (7)$$

For granular soils, the available shear strength is directly proportional to the normal effective stress (σ'), but it is also affected by the density state of the soil:

$$\tau_u = (tan\phi' + \zeta_R(\upsilon_u - \upsilon))\sigma' \quad (8)$$

where ϕ' is the critical state friction angle of the soil, υ is the actual specific volume, υ_u is the correspondent specific volume at failure (or large strains) and ζ_R is a parameter which links the available strength to the density state of the soil. The specific volume at large strain υ_u is generally defined within the critical state framework and it is a common assumption to assume a straight linear relationship between volume and applied stress in the semi-logarithmic compression plane υ-ln σ':

$$\upsilon_u = \Gamma - \lambda \ln(\frac{\sigma'}{\sigma'_{ref}}) \quad (9)$$

where Γ represents the value of υ_u for $\sigma' = \sigma'_{ref}$, λ is the slope of the linear relationship and σ'_{ref} is an arbitrary reference pressure introduced to make equation (9) dimensionally correct. The substitution of equation (9) into equation (8) leads to the following complete definition of the available shear strength:

$$\tau_u = \left(tan\phi' + \zeta_R\left(\Gamma - \lambda \ln\frac{\sigma'}{\sigma'_{ref}} - \upsilon\right)\right)\sigma' \quad (10)$$

3 EXAMINATION OF THE SOIL – FIBRE INTERACTION MECHANISM

3.1 Mobilised fibre stress and fibre-composite strain ratio

Considering the stresses within the pure shear-stress carrying region of the assumed composite model (Fig. 2b), for any fixed value of *x*, it is possible to equate shear forces in annuli of matrix with thickness *z* and obtain the following expression for the shear stress:

$$\tau(z) = \tau_i\left(\frac{r_f}{z}\right) \quad (11)$$

where τ_i is the shear stress at the fibre-soil matrix interface (Fig. 2b).

Rearrangement of equation (6) leads to the following relationship between the shear strain $\gamma(z)$ and shear stress, $\tau(z)$:

$$\gamma(z) = \frac{\partial u}{\partial z}(z) = \frac{\tau(z)\zeta_s}{\tau_u - \tau(z)} \tag{12}$$

where u is the axial displacement of the soil matrix as schematically shown in Fig.1. Equation (11) can be substituted into equation (12) to obtain:

$$\frac{\partial u}{\partial z}(z) = \frac{\tau_i\left(\frac{r_f}{z}\right)\zeta_s}{\tau_u - \tau_i\left(\frac{r_f}{z}\right)} \tag{13}$$

For any fixed value of x, the difference between the displacement u at the location of the axial-stress carrying area ($u_{\bar{R}}$) and that at the fibre/soil interface (u_{r_f}) is given through integration by:

$$\int_{u_{r_f}}^{u_{\bar{R}}} du = \int_{r_f}^{\bar{R}} \frac{\tau_i r_f \zeta_s}{z\left(\tau_u - \tau_i \frac{r_f}{z}\right)}\, dz \tag{14}$$

and following its integration, the relationship below is obtained:

$$u_{\bar{R}} - u_{r_f} = \tau_i \frac{r_f \zeta_s}{\tau_u} \ln\left(\frac{\tau_u \frac{\bar{R}}{r_f} - \tau_i}{\tau_u - \tau_i}\right) \tag{15}$$

At this stage, it is necessary to rearrange equation (15) in order to derive an explicit form of τ_i. While the maximum mobilised interface shear stress τ_i is normally lower than the available shear strength, τ_u, of the soil with $0 < \tau_i < a\tau_u$, (and a<1), it is possible to reasonably approximate the right hand side term in equation (15) by averaging its tangent for τ_i =0 and $\tau_i = a\tau_u$, to give the following linear expression solely in τ_i:

$$\tau_i \frac{r_f \zeta_s}{\tau_u} \ln\left(\frac{\tau_u \frac{\bar{R}}{r_f} - \tau_i}{\tau_u - \tau_i}\right) \approx \tau_i \frac{r_f \zeta_s}{2\tau_u}\left(\ln\left(\frac{\frac{\bar{R}}{r_f} - a}{1-a}\right) + a\left(\frac{\frac{\bar{R}}{r_f} - 1}{\left(\frac{\bar{R}}{r_f} - a\right)(1-a)}\right)\right) \tag{16}$$

Zornberg (2002), using the results of fibre pull-out tests for a range of soils, suggested a value of a around 0.8. Substitution of equation (16) in equation (15) and the subsequent rearrangement leads to an explicit expression for the shear stress at the fibre-soil matrix interface, τ_i:

$$\tau_i = \frac{\left(u_{\bar{R}} - u_{r_f}\right)\tau_u}{r_f \zeta_s \left(\ln\left(\frac{\frac{\bar{R}}{r_f} - a}{1-a}\right) + a\left(\frac{\frac{\bar{R}}{r_f} - 1}{\left(\frac{\bar{R}}{r_f} - a\right)(1-a)}\right)\right)} \tag{17}$$

Attention can now be directed to an element of the fibre such as the one shown in Fig. 2b, where consideration of its equilibrium leads to:

$$\frac{\partial \sigma_f}{\partial x} = -2\frac{\tau_i}{r_f} \tag{18}$$

The account for equation (17), and the following derivation of both terms of equation (18) in ∂x, leads to:

$$\frac{\partial^2 \sigma_f}{\partial x^2} = -\frac{2}{{r_f}^2} \frac{\left(\frac{\partial u_{\bar{R}}}{\partial x} - \frac{\partial u_{r_f}}{\partial x}\right)\tau_u}{\zeta_s \left(\ln\left(\frac{\frac{\bar{R}}{r_f} - a}{1-a}\right) + a\left(\frac{\frac{\bar{R}}{r_f} - 1}{\left(\frac{\bar{R}}{r_f} - a\right)(1-a)}\right)\right)} \tag{19}$$

Since the fibres are considered purely elastic elements, the elasticity theory gives:

$$\frac{\partial u_{rf}}{\partial x} = \frac{\sigma_f}{E_f} \tag{20}$$

while at the far field location (i.e. at the pure axial-stress carrying area):

$$\frac{\partial u_{\bar{R}}}{\partial x} = \varepsilon \tag{21}$$

where ε is the far-field strain of the matrix ideally not affected by fibre-interaction.

Substitution of equations (20) and (21) into (19) leads to the following differential equation:

$$\frac{\partial^2 \sigma_f}{\partial x^2} = \frac{n^2}{{r_f}^2}\left(\sigma_f - E_f \varepsilon\right) \tag{22}$$

with:

$$n = \sqrt{\frac{2\tau_u}{\zeta_s E_f \left(\ln\left(\frac{\frac{\bar{R}}{r_f}-a}{1-a}\right) + a\left(\frac{\frac{\bar{R}}{r_f}-1}{\left(\frac{\bar{R}}{r_f}-a\right)(1-a)}\right)\right)}} \quad (23)$$

The solution of the differential equation (22) can provide the expression of the stress distribution along the fibre:

$$\sigma_f(x) = E_f\varepsilon + Bsinh\left(\frac{nx}{r_f}\right) + Dcosh\left(\frac{nx}{r_f}\right) \quad (24)$$

where *B* and *D* are two constants from the double integration necessary to solve equation (22).

If it is now considered that tensile stresses are developed only along the effective fibre length, l_f^*, the constants *B* and *D* in equation (24) can be removed by imposing the condition of zero mobilised tensile stress, $\sigma_f(x) = 0$, at $x=\pm\, l_f^*/2$, to give:

$$\sigma_f(x) = E_f\varepsilon\left(1 - \frac{cosh\left(\frac{nx}{r_f}\right)}{cosh(ns^*)}\right) \quad (26)$$

where s^* is the effective fibre aspect ratio ($l_f^*/2r_f$). Taking into account that the ratio between the effective and true fibre aspect ratios (s^* and *s* respectively) is equal to the ratio between the effective and true fibre lengths:

$$\frac{s^*}{s} = \frac{l_f^*}{l_f} \quad (27)$$

the average fibre tensile stress can be derived thus:

$$\overline{\sigma_f} = \frac{2}{l_f}\int_0^{l_f^*/2} E_f\varepsilon\left(1 - \frac{cosh\left(\frac{nx}{r_f}\right)}{cosh(ns^*)}\right)dx = E_f\varepsilon\left(\frac{s^*}{s} - \frac{tanh(ns^*)}{ns}\right) \quad (28)$$

where the last term in brackets can be defined as:

$$f_b = \left(\frac{s^*}{s} - \frac{\tanh(ns^*)}{ns}\right) \quad (29)$$

The average fibre tensile strain ($\bar{\varepsilon}_f$) is equal to $\overline{\sigma_f}/E_f$. As a result, the rearrangement of equation (28) shows that the factor f_b is the ratio between the average strain in fibre ($\bar{\varepsilon}_f$) and that in the composite (ε):

$$f_b = \frac{\bar{\varepsilon}_f}{\varepsilon} \quad (30)$$

and it varies between 0 and 1. For a given imposed strain of the composite, the latter condition (f_b =1) sets the maximum theoretical value of the mobilised fibre tensile stress:

$$\sigma_{f\,max} = E_f \varepsilon \quad (31)$$

in which case the f_b factor can also be seen as the ratio between the average mobilised stress in the fibre and this maximum theoretical value (σ_{fmax}). An equivalent factor was successfully considered in constitutive models by Machado et al. (2002) and Diambra et al. (2013) through the use of a simple model constant. In this work, a much more complex formulation of this factor is proposed, taking explicitly into account the fibre length and diameter, soil grain size, fibre and soil stiffnesses, the fibre content and the confinement stress (through the function *n*, equation (23)).

3.2 Analysis of the mobilised fibre stress and f_b factor

The fibre stress distribution (equation (26)) and the sensitivity of the f_b factor (equation (29)), are analysed against the following key variables:

- Fibre length (l_f between 1 and 100 mm)
- Grain size (D_{50} between 0.063 and 2 mm average diameter)
- Fibre stiffness (E_f between 9 and 9000MPa)
- Confining stress level (σ'_z from 10 to 1000kPa)

The analysis is conducted for a fixed fibre content, w_f, of 0.3%, by dry mass of sand and a fibre diameter of 0.1mm. A summary of the variables alongside the assumed soil model constants ($\phi', \lambda, \Gamma, \zeta_R, \zeta_s$), fibre model constants (E_f, k), and soil specific volume, υ, are given in Table 1.

Table 1. Summary of fibre and soil properties, model constants and stress level condition used in the parametric investigation

Sand matrix properties	*D50*	*0.063; 0.2; 0.63; 2 mm*
	υ	*2*
Soil model constants	ϕ'	*35°*
	λ	*0.031*
	Γ	*2.13*
	ζ_s	*0.005*
	ζ_R	*0.5*
Fibres properties	l_f	*1; 10; 50; 100 mm*
	d_f	*0.1 mm*
	w_f	*0.3%*
Fibre model constants	E_f	*90; 900; 9000; 90000 MPa*
	k	*1*
Composite confining stress	σ'_z	*1; 10; 100;1000 kPa*

3.2.1 Fibre length and grain size dimensional group effects

The distribution of the mobilised fibre tensile stress against the position along the fibre, both normalised respectively by the maximum theoretical tensile stress σ_{fmax} (equation (31)) and the effective fibre length, l_f^*, is shown in Fig. 4. The simulations are performed for fixed fibre stiffness E_f = 900MPa and confining stress σ'_z = 100 kPa. The fibre length effect for a fixed mean grain size D_{50}=0.063mm is shown in Fig. 4a. As expected, for all the simulations the tensile stresses are null at the fibre ends and gradually increase towards the central region, where a maximum is reached. It is clear that, above a certain fibre length, the tensile stress in the central region of the fibre effectively approaches the maximum allowable value (σ_{fmax}**)** which signifies full fibre soil interaction. However, the effect of l_f on the fibre stress distribution is directly related to two non-dimensional groups: the fibre aspect ratio, *s*, and fibre length to mean grain size ratio, l_f/D_{50}, and the results in this Fig. 4a cannot discriminate their individual contribution. However, the effect of the l_f/D_{50} ratio can be singled out in Fig. 4b which shows a series of simulation results performed for a range of grain sizes and for fixed fibre length (l_f) and aspect ratio (*s*). The mobilised tensile stress remains extremely low for large grains (low l_f/D_{50} ratios) but gradually increases with the decreasing of the particle size and, as the grain size becomes smaller and smaller, it appears to converge to a limiting curve that corresponds to the case when the effective

fibre aspect ratio (s*) equals k times the real fibre aspect ratio ($k \cdot s$, see equations 4 and 27). As shown in Figure 4b, the effective fibre aspect ratio s* for the cases of smaller grain size diameters, s*=94 and s*= 99, is very close to product $k \cdot s$ = 100, with s=100 and k=1 for this parametric exercise, which signifies an efficient use of fibre dimensions. This is strongly noticeable if the variation of the strain ratio, f_b, is plotted with the fibre length to grain size ratio (l_f/D_{50}) (Fig. 5a). Data for s=100 extracted from Fig 4b are also indicated by the use of their corresponding markers. It seems that, as also previously suggested by Michałowski and Čermák (2003), the length of the fibres needs to be at least 10 times the average grain size to ensure some development of the fibre soil interaction mechanism. On the other hand, the trend of f_b with the aspect ratio shown in Fig.5b suggests that the onset of the interaction is expected to occur for values of the aspect ratio between 10 and 100 depending on the soil grain size, but higher values would be recommended to ensure an efficient interaction.

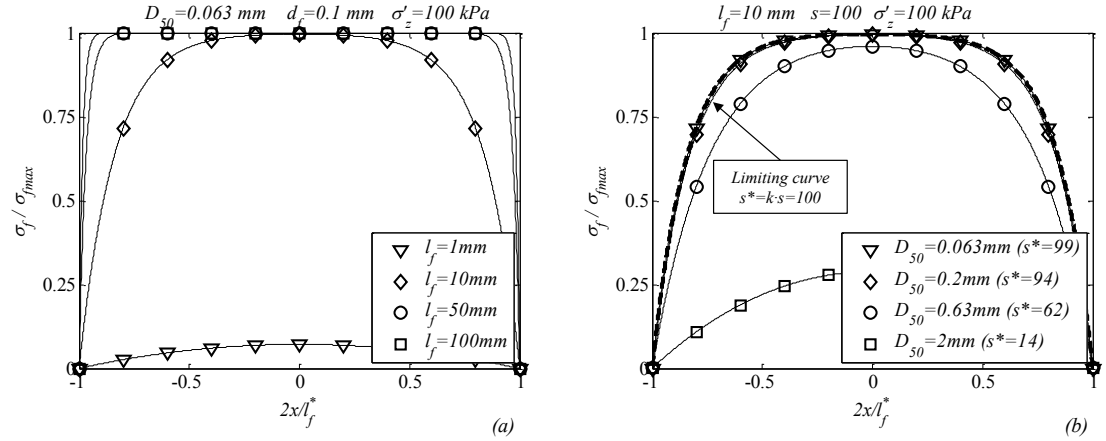

Fig. 4 Influence of *(a)* fibre length and *(b)* mean grain size on fibre normalised

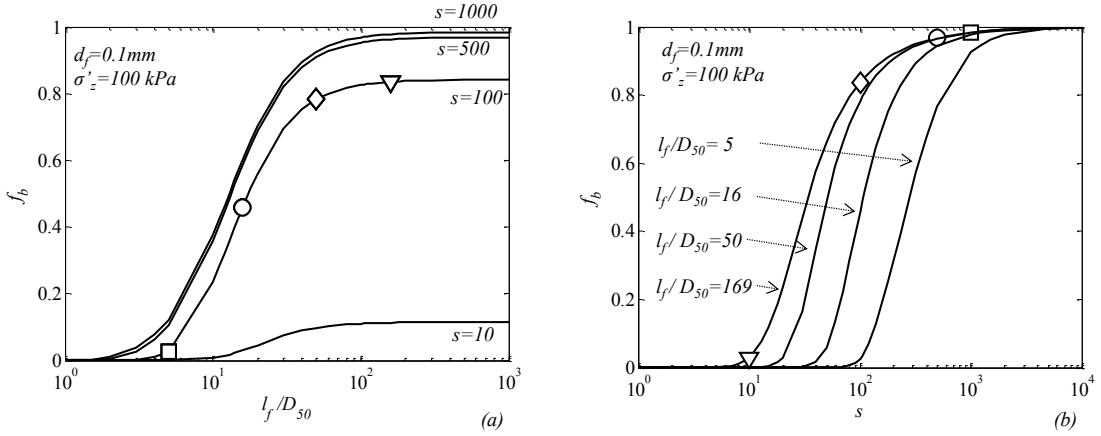

Fig.5 Variation of the efficiency factor f_b (a) with l_f/D_{50} and different fixed s values and (b) with aspect ratio s for different l_f/D_{50} ratios.

3.2.2 Fibre stiffness

Fig 6a shows the normalised stress distribution along the fibre length for a range of fibre stiffnesses as given in Table 1, for a confining stress σ'_z = 100 kPa, and fixed fibre length l_f=10mm and mean grain size D_{50}=0.63mm. Increasing the stiffness of the fibres apparently has an adverse effect on the normalised stress, suggesting a less effective interaction mechanism between the fibre and the soil with a decreasing value of the bracket term in equation (26). However, this may be a misleading observation because the effective mobilised stress in the fibre σ_f is actually the direct product between this bracket term and E_f, and, for typical applications, the fibre stiffness still retains a dominant weight. The variation of the f_b factor with the fibre stiffness normalised by the soil shear stiffness (G=14 MPa) derived from equation (7) is shown in Fig.6b for a range of l_f/D_{50} ratios and fixed fibre aspect ratio s. The f_b factor increases with the l_f/D_{50} ratio, but for a given l_f/D_{50} it retains its value up to a fibre stiffness of the same order of magnitude as soil shear stiffness. Unavoidably, the mobilised strain in the fibre decays with the increase in the contrast between the fibre and soil stiffness. Referring to previous Fig.1, higher fibre stiffness would induce larger shear distortions in the matrix and a larger mismatch of the strain fields between the constituents.

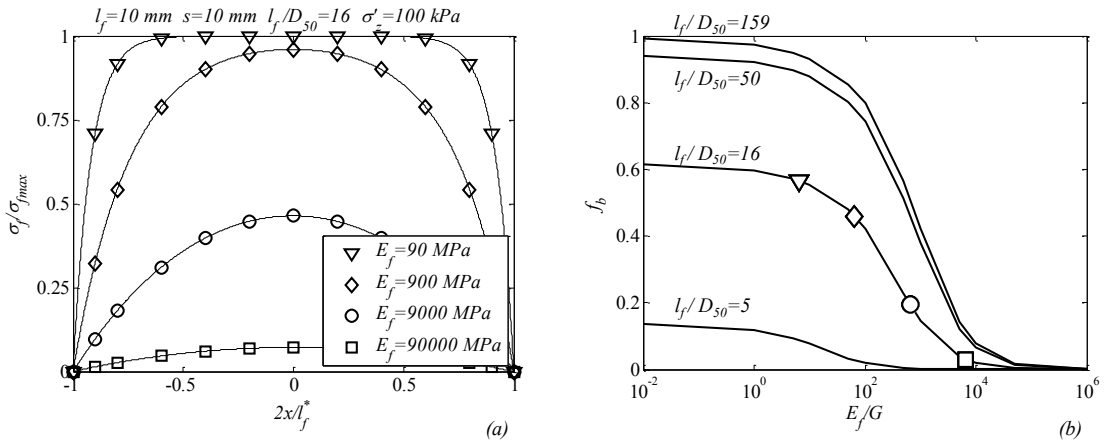

Fig.6 *(a)* Influence of fibre stiffness E_f on the normalised stress distribution along the fibre and *(b)* trend of f_b versus E_f/G for a range of l_f/D_{50} ratios.

3.2.3 Stress level

Fig. 7a shows the normalised stress distribution along the fibre length for a range of confining stress levels (Table 1), and fixed fibre length l_f=10mm, mean grain size D_{50}=0.063mm and E_f =9000 MPa. The normalised stress distribution is highly affected by the stress level as experimentally observed by Diambra et al. (2010) among others. An increase in the stress level corresponds to an increase in the soil shear stiffness and, in accord with current developments, a decrease of the ratio E_f/G induces larger strains in the fibre for a given strain the composite, as also shown in Fig. 6b. The f_b factor increases with the stress level (Fig. 7b) but, as expected, slender fibres mobilise higher strains for a fixed confinement stress level. One aspect that may occur in the case of fibre reinforced soils is the low level of confinement expected, in which case the mobilisation of strains and stresses in the fibre must be controlled by other factors like fibre aspect ratio and fibre length to mean grain size ratio, l_f/D_{50}.

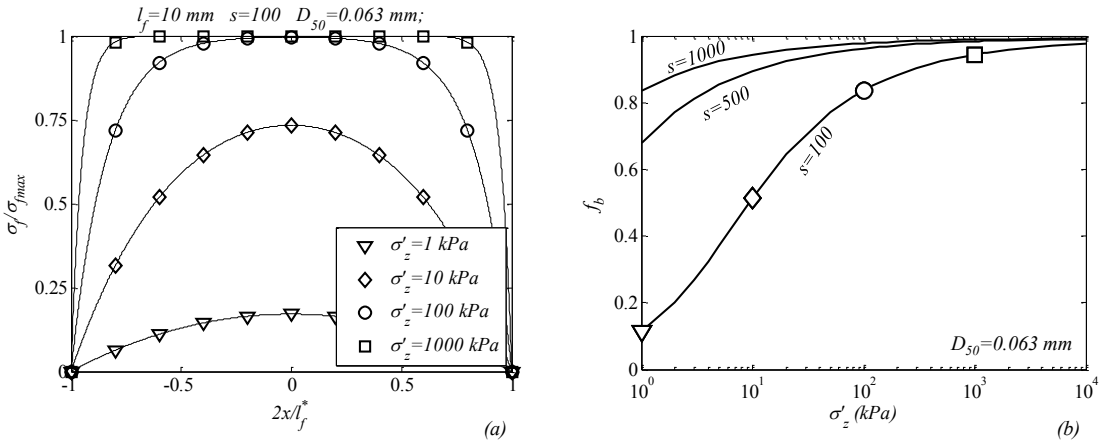

Fig.7 *(a)* Influence of stress level on the normalised stress distribution along the effective fibre length and *(b)* trend of f_b versus stress level for a range of fibre aspect ratios.

4 IMPLEMENTATION IN A CONSTITUTIVE MODEL

The implementation of the proposed developments into a constitutive model is further explored here. The account for the effects of the fibre and grain sizes and stress level on the fibre–soil strain transfer mechanism is controlled through the introduction of the proposed expression for the factor f_b (equation (29)). The adopted baseline model is that proposed by Diambra et al. (2013) and some of its key features are presented below. The modelling framework, based on the superimposition of the effects of the fibre and the sand matrix, accounts for fibre orientation and introduces failure mechanisms such as fibre-matrix slippage (or pull-out) and fibre breakage through capping and/or removing the fibre contribution if some pre-imposed controlling conditions like fibre/matrix interface friction resistance or fibre tensile strength are reached. From the force equilibrium of a fibre reinforced element, the following relationship between incremental stresses in the composite and in the constituent phases was determined:

$$\dot{\boldsymbol{\sigma}}^* = \mu_m \dot{\boldsymbol{\sigma}}' + \dot{\mu}_m \boldsymbol{\sigma}' + \mu_f \dot{\overline{\boldsymbol{\sigma}}}_f + \dot{\mu}_f \overline{\boldsymbol{\sigma}}_f \tag{32}$$

where $\boldsymbol{\sigma}^*$ is the incremental stress state of the composite, $\boldsymbol{\sigma}'$ is the stress state of the sand and $\overline{\boldsymbol{\sigma}}_f$ is the overall stress contribution of the fibre phases, while μ_m and μ_f are the volumetric concentrations of the

sand matrix and fibres respectively. Bold quantities represent vectors, while the dotted symbol denotes incremental quantities.

The relationship in equation (32) can be expanded to consider appropriate constitutive models for the sand and the fibres. Thus, introducing the stiffness matrices $[\boldsymbol{M_m}]$ and $\left[\boldsymbol{M_f}\right]$, it is possible to obtain:

$$\dot{\boldsymbol{\sigma}}^* = \mu_m[\boldsymbol{M_m}]\dot{\boldsymbol{\varepsilon}}_{\boldsymbol{m}} + \dot{\mu}_m\boldsymbol{\sigma}' + \mu_f\left[\boldsymbol{M_f}\right]\dot{\bar{\boldsymbol{\varepsilon}}}_{\boldsymbol{f}} + \dot{\mu}_f\overline{\boldsymbol{\sigma}}_f \tag{33}$$

where $\dot{\boldsymbol{\varepsilon}}_{\boldsymbol{m}}$ and $\dot{\bar{\boldsymbol{\varepsilon}}}_{\boldsymbol{f}}$ are the incremental strain tensors for the sand and fibre phases respectively. Under the assumption that the overall deformation undergone by the fibre phase during loading is negligible compared with that undergone by the sand matrix, it is possible to assume that (Diambra et al., 2013):

$$\dot{\boldsymbol{\varepsilon}} \approx \mu_m\dot{\boldsymbol{\varepsilon}}_{\boldsymbol{m}} \tag{34}$$

While, according to the previous developments, the following relationship for the strain in the fibres can be assumed:

$$\dot{\bar{\boldsymbol{\varepsilon}}}_f = f_b\dot{\boldsymbol{\varepsilon}} \tag{35}$$

The overall incremental stress-strain relationship for the composite material becomes:

$$\dot{\boldsymbol{\sigma}}^* = [\boldsymbol{M_m}]\dot{\boldsymbol{\varepsilon}} + \mu_f\left[\boldsymbol{M_f}\right]f_b\dot{\boldsymbol{\varepsilon}} + \dot{\mu}_m\boldsymbol{\sigma}' + \dot{\mu}_f\overline{\boldsymbol{\sigma}}_f \tag{36}$$

There is complete freedom in choosing the constitutive model for the sand matrix and thus the stiffness matrix $[\boldsymbol{M_m}]$. However, following Diambra et al. (2013), the Severn-Trent sand model (Gajo and Muir Wood, 1999) has been adopted.

On the other hand, the fibres have been considered as elastic elements which react only in extension. The stiffness matrix $\left[\boldsymbol{M_f}\right]$ accounts for the response of the overall fibre phase, and it should account for the distribution of fibre orientation. A smearing procedure has been proposed by Diambra et al. (2013) and Diambra and Ibraim (2013) and the stiffness matrix for elastic fibre can be written as follows:

$$\left[\boldsymbol{M_f}\right] = \frac{E_f\pi}{v_f}[\boldsymbol{M_\theta}] \tag{37}$$

where $[\boldsymbol{M_\theta}]$ accounts for the distribution of fibre orientation within the soil matrix , and the definition of this term is provided by Eqs. (23), (25) and (26) in Diambra et al. (2013). The parameter υ_f is a model constant defining the specific volume of the fibre phase.

It is finally possible to demonstrate that the incremental variation of the volumetric concentrations can be linked to the strain in composite by:

$$\dot{\mu}_m = -\mu_f tr(\dot{\boldsymbol{\varepsilon}}) \quad , \quad \dot{\mu}_f = \mu_f tr(\dot{\boldsymbol{\varepsilon}}) \tag{38}$$

and the unique incremental stress-strain relationship for the composite material thus becomes:

$$\dot{\boldsymbol{\sigma}}^* = \left([\boldsymbol{M_m}] + \mu_f \frac{E_f \pi}{\upsilon_f}[\boldsymbol{M_\theta}] f_b\right)\dot{\boldsymbol{\varepsilon}} + \mu_f\left(\overline{\boldsymbol{\sigma}}_f - \boldsymbol{\sigma}'\right) tr(\dot{\boldsymbol{\varepsilon}}) \tag{39}$$

5 SIMULATION OF ELEMENT TEST RESULTS AND DISCUSSION

5.1 Materials, specimen preparation and experimental programme

In order to challenge the proposed modelling developments, a number of triaxial laboratory tests on two types of sands (Hostun RF sand and Leighton Buzzard sand Fraction *B*) reinforced with discrete flexible polypropylene fibres have been carried out. The two types of sand are characterised by different mean grain sizes (D_{50}=0.32 and 0.85 mm), while the fibres have been cut at four different lengths (l_f=6 mm, 12 mm, 23 mm and 35 mm) to investigate the effect of both fibre length and grain size geometrical variables on the fibre-sand interaction mechanism. Further details of the fibres and sand used in this investigation are given in Table 2.

Table 2. Properties of the Hostun RF (S28) and Leighton Buzzard sands and the polypropylene fibres used in this investigation.

		Hostun RF (S28) sand	Leighton Buzzard sand
D_{50}	*Mean grain size*	0.32	0.85
C_u	*Coeff. uniformity*	1.62	1.38
C_g	*Coeff. gradation*	1	1.09
e_{max}	*Max void ratio*	1	0.802
e_{min}	*Min void ratio*	0.62	0.506
Gs	*Specific gravity*	2.65	2.65

Fibres		
l_f	*Length*	6-12-23-35 mm
d_f	*Diameter*	0.1 mm
σ_{ften}	*Tensile strength*	225 MPa
G_f	*Specific gravity*	0.91
E_f	*Elastic modulus*	900 MPa

Table 3 - List of triaxial tests used for model validation

Test name	l_f*(mm)*	σ_c *(kPa)*	*e*	q_{20} *(kPa)*	φ'_{20} *(°)*
H100FL0	0	100	0.909	301.2	36.6
H100FL6	6	100	0.917	353.4	39.0
H100FL12	12	100	0.900	451.1	42.6
H100FL23	23	100	0.900	489.3	44.6
H100FL35	35	100	0.912	517.2	45.4
H200FL0	0	200	0.914	543.0	35.1
H200FL6	6	200	0.903	603.2	36.7
H200FL12	12	200	0.900	670.6	38.6
H200FL23	23	200	0.900	748.2	40.5
H100FL35	35	200	0.914	803.3	41.6
LB100FL0	0	100	0.735	317.6	37.3
LB100FL6	6	100	0.744	329.7	38.4
LB100FL12	12	100	0.752	359.3	39.5
LB100FL23	23	100	0.748	438.2	42.5
LB100FL35	35	100	0.739	488.5	44.4
LB200FL0	0	200	0.740	532.7	34.5
LB200FL6	6	200	0.744	577.3	36.0
LB200FL12	12	200	0.744	639.1	37.6
LB200FL23	23	200	0.744	715.6	39.8
LB200FL35	35	200	0.739	755.3	40.7

The cylindrical specimens to be tested in the triaxial apparatus have been prepared using the moist tamping technique (Ladd, 1978) and employing three layers of equal height. A detailed description of

the sample fabrication procedure can be found in Diambra et al. (2010). Samples of 70 mm diameter and 70 mm height were tested using enlarged lubricated ends for trying to preserve the homogeneous cylindrical shape even at the largest possible axial strains, about 20%. Additional details of the testing procedure, apparatus and loading conditions can also be found in Ibraim et al. (2011). The conventional triaxial compression tests were performed on fully consolidated loose specimens (relative density D_r≈20-25%) under constant confining cell pressures of 100 and 200 kPa. A unique fibre content w_f=0.3% was adopted for the reinforced specimens. Tests on unreinforced sand samples were also performed. A list of the performed tests is provided in Table 3 where the cell confining pressure (σ_c), void ratio after consolidation (e), deviatoric strength (q_{20}), and friction angle (φ'_{20}) at 20% axial strain are reported. Note that the void ratio considers the fibres as part of solids. In the test name, the first letters LB or H refer to Leighton Buzzard or Hostun sand respectively.

5.2 Model parameters

The model parameters adopted in this simulation exercise are summarised in Table 4. The parameters relative to the sand matrices have been calibrated on the unreinforced sample results. There are two parameters which require to be calibrated for the fibre phase: the specific volume v_f of the fibres which have been assumed here to be equal to 3.27 as resulted after calibration in Diambra et al. (2013) and the value k on the definition of the maximum effective length in equation (4). This parameter has been calibrated to have a reasonable match of the stress–strain behaviour for the longer fibre. Finally, it is also necessary to define a distribution of fibre orientation. Diambra et al. (2007) and Ibraim et al. (2012) have demonstrated that the employed moist tamping technique for sample preparation induces a rather preferred horizontal bedding orientation of fibres and that the distribution of fibre orientation in the investigated specimens can be represented by the following function:

$$\rho(\theta) = (A_\theta + B_\theta |cos^{n_\theta}\,\theta|) \tag{40}$$

where A_θ = 0, n_θ = 5 and B_θ = 0.324 are constant coefficients which have been experimentally determined and θ is the inclination from an horizontal plane. The link between equation (40) and the stiffness matrix $\mathbf{[M_\theta]}$ is given by equation (23) in Diambra et al. (2013).

Table 4. Summary of assumed model parameters for the simulation exercise

Sand matrix			
Parameter	Description	Value for Hostun Sand	Value for Leigthon Buzzard Sand
C	Ratio of elastic shear modulus to dynamic shear modulus	0.4	0.4
v	Poisson' s ratio	0.1	0.1
ϕ'	Critical-state friction angle	34°	35°
Γ	Intercept for critical-state line on υ_m- ln p' plane at p'=1 kPa	2.13	2.08
λ	Slope of the critical-state line on υ_m- ln p' plane	0.031	0.031
k_r	Link between changes in state parameter and current strength	1.5	1.5
B	Parameter controlling hyperbolic stiffness relationship	0.0025	0.0025
R_y	Ratio of size of yield and strength surfaces	0.1	0.1
A	Multiplier in flow rule	0.75	0.75
k_d	State parameter contribution in flow rule	1.5	1.5
Sand-fibre interaction			
Parameter	Description	Value for Hostun Sand	Value for Leigthon Buzzard Sand
k	Maximum ratio between effective and actual fibre length	0.6	0.5
Fibres			
Parameter	Description	Value	
E_f	Elastic modulus	900	
υ_f	Specific volume of the fibres	3.27	

5.3 Model simulations and discussion

The comparison between the model simulations and the experimental results in terms of deviatoric stress-strain and volumetric behaviour for the triaxial tests performed at 100 kPa of cell confining pressure are reported in the following Figs. 8 and 9 for Hostun sand and Leighton Buzzard sand

respectively. The deviatoric stress-strain trends suggest that the model captures well the general trend of increasing fibre effectiveness with increasing length. On the volumetric plane, the model captures the increased dilation experimentally observed for reinforced specimens. While the experimental results do not show any particular volumetric trend with the fibre length, because small variation in the fabrication void ratio may have a quite considerable effect on the volumetric response, the model depicts a decreased dilation with increasing fibre length, naturally owed to the increased confinement effect associated with longer fibres.

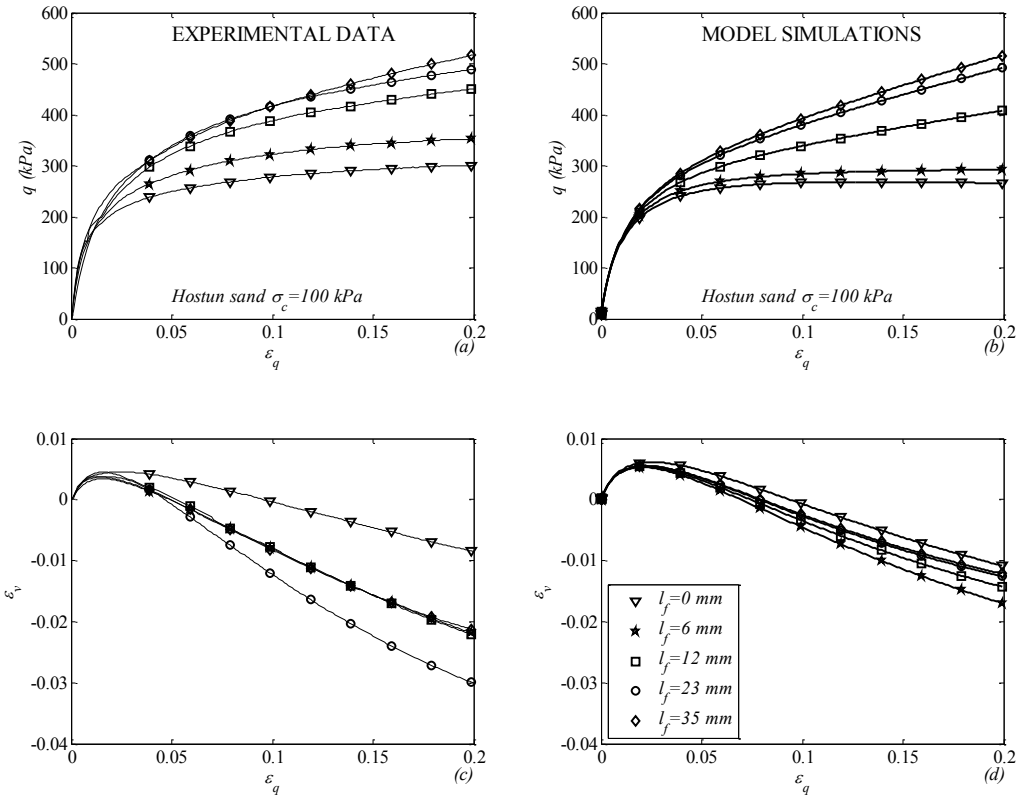

Fig. 8 Triaxial test results and model simulations for Hostun sand unreinforced and reinforced (0.3% fibre content) specimens, tested under 100 cell confining pressures (legend indicates the fibre length).

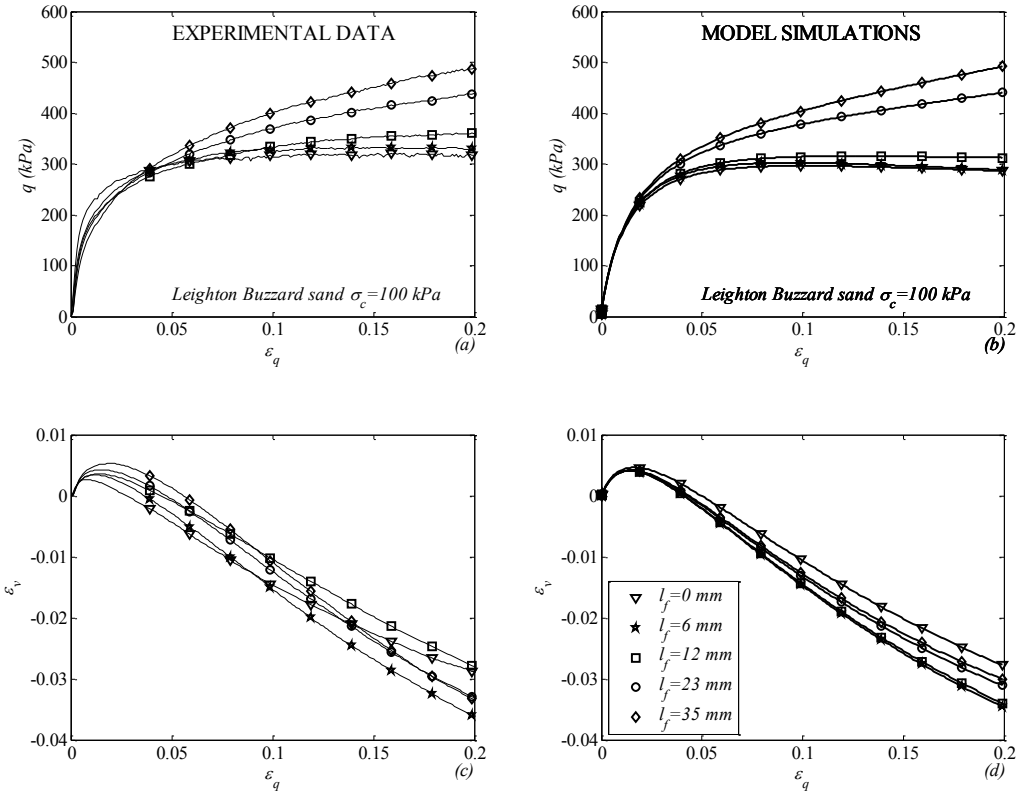

Fig. 9 Triaxial test results and model simulations for Leighton Buzzard sand unreinforced and reinforced (0.3% fibre content) specimens, tested under 100 kPa cell confining pressures (legend indicates the fibre length).

In order to estimate the real capabilities of the proposed developments, the comparison between model simulations and experimental results is analysed in terms of the additional deviatoric strength of the reinforced samples. For a fixed strain level, the term Δq can be defined as:

$$\Delta q = q_r - q_u \tag{41}$$

where q_r and q_u are the deviatoric stresses for a reinforced and the respective unreinforced specimens tested under the same conditions. In this way, it is possible to remove some of the inaccuracies related to simulation of the reference unreinforced sand behaviour and analyse the predicted contribution of the fibres. The comparisons are shown in Fig. 10 for both sands and both employed confining pressures. It is clear that the model simulation predicts well the magnitude of increased strength with the increase of the length of the fibres. This is due to the increase in mobilised fibre stress and strain ratio factor f_b which was observed with both increase in aspect ratio and increase of the l_f/D_{50} ratio, reported in the

previous Fig. 5. On the other hand, while the predicted additional fibre strength contribution appears to increase linearly with the deviatoric strain, the experimental results show a more curvilinear trend with even a decrease in deviatoric strength in the initial phase of loading. This trend is more visible for the coarser sand. Knowing that fibres need strain to start mobilising any tensile stress, a delayed fibre reinforcement effect is fully expected.

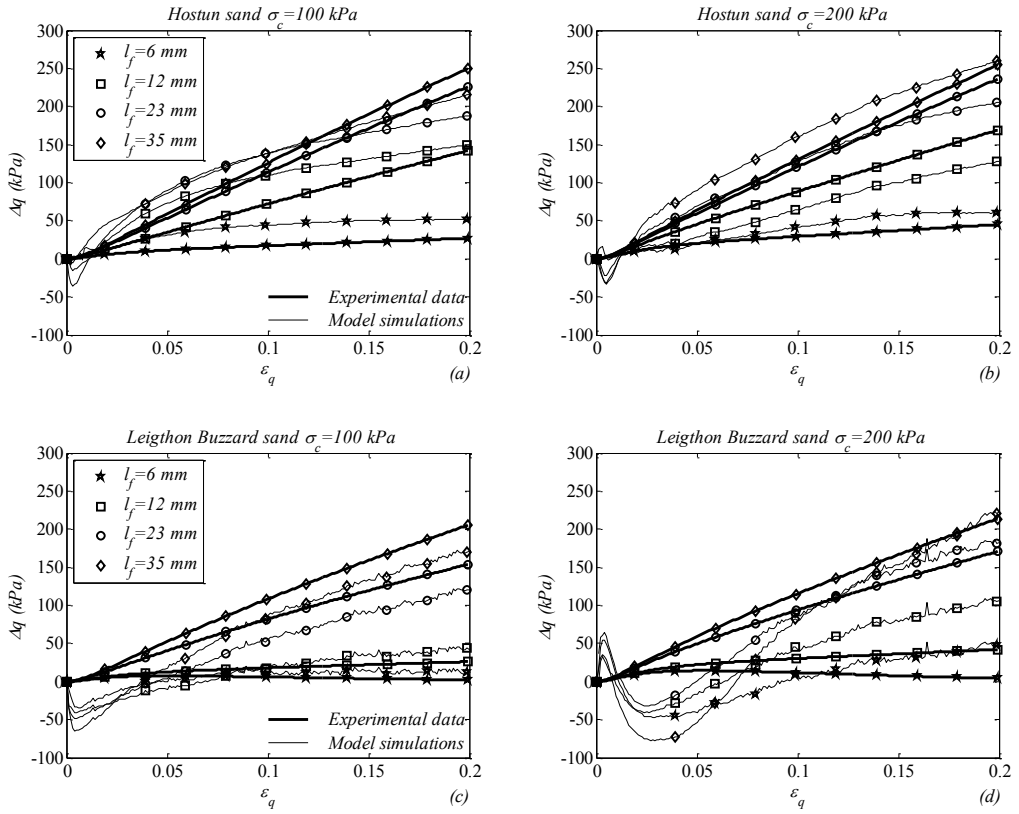

Fig. 10 Comparisons between net deviatoric contributions for reinforced (0.3% fibre content) specimens of Hostun and Leighton Buzzard sands, under two testing confining pressures (legend indicates the fibre length).

The comparison proposed in Fig.11 between the predicted and the measured increased deviatoric strength at 20% deviatoric strain (Δq_{20}) highlights the power of the modelling developments able to capture the complex behaviour of fibre reinforced soil. The measured increase in deviatoric strength is not linearly proportional to the fibre content but has a somewhat "s" shape which is well depicted by the model. Comparison between Fig.11a and 11b also suggests that the fibre contribution is a bit larger for the finer soil, as demonstrated by the parametric study on the efficiency factor *w*ith l_f/D_{50} reported

earlier (Fig. 5). Finally, Fig. 11 also shows that the model is able to predict the increase in the net fibre contribution with increased stress level, which is due to the enhanced fibre-soil interaction shown previously in Fig.7.

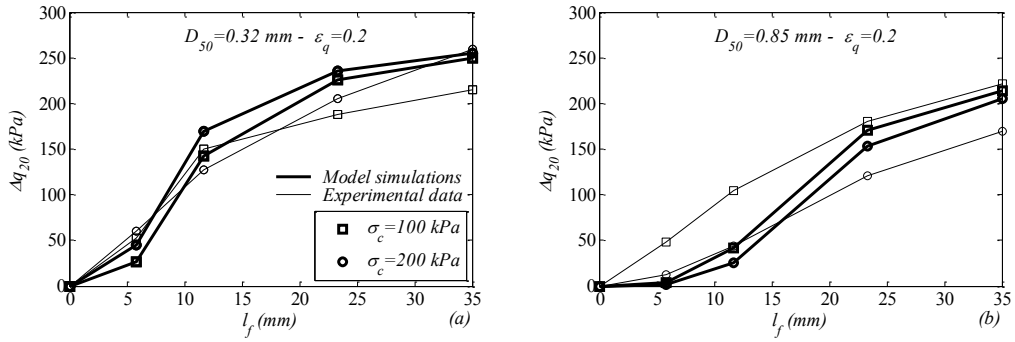

Fig.11 Comparisons of trends of net deviatoric contributions versus length of fibres for reinforced (0.3% fibre content) specimens of Hostun and Leighton Buzzard sands, under two testing confining pressures (legend indicates the cell confining pressure).

6 CONCLUSIONS

A description of the local fibre-soil stress-transfer mechanism for fibre-reinforced granular soils based on a modified shear lag theory is presented. The theory allows for the development of an analytical expression of the stress distribution along the fibre, which can explicitly account for the effects of the geometrical fibre and granular size characteristics, including also the fibre stiffness, global stress level, soil density, and the non-linearity of the soil behaviour. The integration of the stress distribution function also allows the derivation of the factor f_b which represents the strain ratio between the fibre and the composite and takes explicitly into account the same range of parameters. The parametric study that follows provides valuable insight into the internal interaction mechanism. The following conclusions can be drawn:

- The fibre length plays a major role in the interaction process, but the actual fibre length needs to be at least 10 times the average grain size to ensure a triggering of the interaction mechanism.

- Finer granular soils generate much more effective interactions, whereas, depending on the grain size, the onset of the interaction mechanism requires fibre aspect ratios between 10 and 100. For a given soil, the analysis provides a tool for an effective control for an efficient use of fibre dimensions.
- The f_b factor decreased with the increase of the fibre stiffness, but the mobilised fibre stress remains important and should still govern the overall strength increase.
- For a given fibre stiffness and composite strain, the increase in the soil stiffness induced by an increase in the soil confinement results in an increase of the factor f_b and thus in larger stress mobilised in the fibres.

The scale-up of the problem at the composite level is then conducted by using a continuum constitutive model (Diambra et al., 2013) modified to account for the strain ratio between the fibre and the composite, factor f_b. The model is assessed against a series of triaxial compression tests on two different sands mixed with polypropylene fibres of different aspect ratios. The validity of the proposed developments, which include the key assumption on the effective fibre length, is clearly emphasised.

The proposed research work on fibre-reinforced sand soils, while fundamental in nature, provides not only a detailed analysis of the role played by various parameters, but also a tool that can be used efficiently in the design processes of such complex materials.

ACKNOWLEDGMENTS

This work has been supported by the EPSRC grant EP/J010022/1. The Authors would like to thank Dr C. Sandru for valuable comments on the paper structure and editorial suggestions.

7 REFERENCES

Al Refeai, T.O. (1991). Behaviour of granular soils reinforced with discrete randomly oriented inclusions. *Geotextiles and Geomembranes* **10**, 319-333.

Aveston, J. & Kelly, A. (1973). Theory of multiple fracture of fibrous composites. *Journal of Materials Science* **8**, 352–362.

Budiansky, B., Hutchinson, J.W. and Evans, A.G. (1986). Matrix fracture in fiber-reinforced ceramics. *Journal of the Mechanics and Physics of Solids* **34**, No. 2, 167–189.

Consoli, N.C., Casagrande, M.D.T. and Coop, M.R. (2005). Effect of fiber reinforcement on the isotropic compression behavior of a sand. *Journal of Geotechnical and Geoenvironmental Engineering* **131**, No. 11, 1434-1436.

Consoli, N.C., Heineck, K.S. and Casagrande, M.D.T. (2007). Shear strength behavior of fiber-reinforced sand considering triaxial tests under distinct stress paths. *Journal of Geotechnical and Geoenvironmental Engineering*, **133**, No. 11, 1466-1469.

Cox, H.L. (1952). The elasticity and strength of paper and other fibrous materials. *British Journal of Applied Physics* **3**, 72–79.

De Gennes, P.G. (1979). *Scaling concepts in Polymer Physics*, 1st edn. Cornell University Press.

Diambra, A., Russell, A.R., Ibraim, E., and Muir Wood, D. (2007). Determination of fibre orientation distribution in reinforced sand. *Géotechnique* **57**, No. 7,623–628. doi:10.1680/geot.2007.57.7.623.

Diambra, A., Ibraim, E., Muir Wood, D. and Russell, A.R. (2010). Fibre Reinforced Sands: Experiments and Modelling. *Geotextiles and Geomembranes* **28**, 238–250. doi:10.1016/j.geotexmem.2009.09.010.

Diambra, A., Ibraim, E., Muir Wood, D., Russell, A.R. (2013). Fibre reinforced sands: from experiments to modelling and beyond. *International Journal Numerical and Analytical Methods in Geomechanics* **37**, 2427–2455.

Diambra, A. & Ibraim, E. (2013). Modelling of fibre cohesive soil mixtures. *Acta Geotechnica*, Published on-line. DOI 10.1007/s11440-013-0283-y

Gajo, A. & Muir Wood, D. (1999). Severn-Trent sand: a Kinematic hardening constitutive model: the q-p formulation. *Géotechnique* **49**, No. 5, 595–614.

Gray, D.H. & Ohashi, H. (1983). Mechanics of fiber reinforcement in sands. *Journal of Geotechnical Engineering* ASCE **109**, No.3, 335–353

Gray, D.H. & Al-Refeai, T. O. (1986). Behaviour of fabric - versus fiber-reinforced sand, *Journal of Geotechnical Engineering* ASCE **112**, No. 8, 804.820.

Hull, D. & Clyne, T. W. (1996). *An introduction to composite materials*, 2nd edn. Cambridge solid state science series.

Ibraim, E., Muir Wood, D. and Maeda, K. (2006). Fibre-reinforced granular soils behaviour: numerical approach**.** *Proc. Int. Symp. Geomechanics and Geotechnics of Particulate Media, Ube, Yamaguchi, Japan* 12-14. *Hyodo, E. M., Murata, H. & Nakata, Y. (eds.). Taylor & Francis Group,* 443 – 448.

Ibraim, E., Diambra, A., Muir Wood, D. and Russell, A.R. (2010).Static liquefaction of fibre reinforced sand under monotonic loading. *Geotextiles and Geomembranes* **28**, 374–385.

Ibraim, E, Diambra A, Russell AR, Wood DM (2012). Assessment of laboratory sample preparation for fibre reinforced sands. *Geotextiles and Geomembranes* **34**, 69–79.

Ladd, R. S. (1978). Preparing specimens using undercompaction. *Geotechnical Testing Journal* **1**, No. 1, 16–23.

Lirer, S., Flora, A. and Consoli, N.C. (2011). On the strength of fibre-reinfroced soils. *Soils and Foundations* **51**, No.4, 601–610.

Machado, S.L., Carvalho, M.F. and Vilar, O. (2002). Constitutive model for municipal solid waste. *Journal of Geotechnical & Geoenvironmental Engineering ASCE* **128**, No.11, 940–951.

Maeda, K., & Ibraim, E. (2008). DEM analysis of 2D fibre-reinforced granular soils. *Proc. Int. Symp. Deformation Characteristic of Geomaterials*, IS-Atlanta 2:623–628.

Maher, M.H. & Gray, D.H. (1990). Static response of sand reinforced with fibres. *Journal of Geotechnical Engineering* ASCE **116**, No. 11, 1661–1677.

Mahesh, S., Hanan J.C., Ustundag, E. and Beyerlein, I.J. (2004). Shear-lag model for a single fiber metal matrix composite with an elasto-plastic matrix and a slipping interface, *International Journal of Solids and Structures* **41**, 4197–4218.

Michałowski RL, Cermák J. (2003). Triaxial compression of sand reinforced with fibers, *Journal of Geotechnical and Geoenvironmental Engineering* ASCE **129**, No.2, 125–136.

Muir Wood, D. (2009). *Soil Mechanics: A one-dimensional introduction*. Cambridge University Press.

Ranjan, G., Vasan, R.M. and Charan, H.D., (1996). Probabilistic analysis of randomly distributed fiber-reinforced soil. *Journal Geotechnical Engineering* ASCE **122**, No. 6, 419-426.

Zornberg, J. G. (2002). Discrete framework for limit equilibrium analysis of fibre-reinforced soil. *Géotechnique* **52**, No. 8, 593–604.